Photofragment imaging of HNCO decomposition: Angular anisotropy and correlated distributions

A. Sanov,[a] Th. Droz-Georget, M. Zyrianov, and H. Reisler[b]
Department of Chemistry, University of Southern California, Los Angeles, California 90089-0482

(Received 19 November 1996; accepted 22 January 1997)

Photodissociation of jet-cooled isocyanic acid has been examined by photofragment ion imaging of H(D) from H(D)NCO and CO from HNCO, and by laser induced fluorescence (LIF) of NH($a\ ^1\Delta$) from HNCO. Only modest recoil anisotropy is observed in the H+NCO channel at 243.1 nm ($\beta=-0.13\pm0.05$), while the D+NCO channel at approximately the same wavelength reveals no anisotropy ($\beta=0.00\pm0.05$), confirming that the dissociation of H(D)NCO from the opening of the H(D) channel proceeds via vibrational predissociation on the $S_0(^1A')$ surface. In contrast, substantial anisotropy ($\beta=-0.66\pm0.08$) is observed in the NH($a\ ^1\Delta$)+CO channel at 230.1 nm, but this value can correspond to dissociation on either S_0 or S_1. The photolysis region between 243 and 230 nm thus appears important in providing clues to the dissociation mechanism and the competition between different potential energy surfaces. At 217.6 nm, product state distributions exhibit clear dynamical biases. CO is produced in both $v=0$ and $v=1$, while NH($a\ ^1\Delta$) distributions correlated with different rovibrational levels of CO, although different in shape, are always cold, consistent with the global NH distribution measured by LIF. The NH distributions indicate dissociation on $S_1(^1A'')$, and can be described by Franck–Condon mapping of transition state wave functions in the HNC bending coordinate without additional torque, implying little anisotropy in the potential along that coordinate. On the other hand, a larger torque is manifest in the CO rotational distribution. Although at 217.6 nm the dissociation is likely to be dominated by decomposition on S_1, competition with radiationless decay is still manifest. From analysis of the CO photofragment velocity distribution at 230.1 nm, the NH($a\ ^1\Delta$)+CO dissociation threshold is determined at 42 765 ± 25 cm^{-1}. © *1997 American Institute of Physics.* [S0021-9606(97)00517-5]

I. INTRODUCTION

The photodissociation of HNCO following excitation to the $S_1(^1A'')$ state has recently attracted much attention, as it involves a small molecule which nevertheless can dissociate via three channels evolving on two or three potential energy surfaces (PES's),[1–14]

$$\rightarrow \mathrm{NH}(X\ ^3\Sigma^-)+\mathrm{CO}(X\ ^1\Sigma^+) \quad (1)$$

$$\mathrm{HNCO}\rightarrow \mathrm{H}(^2S)+\mathrm{NCO}(X\ ^2\Pi) \quad (2)$$

$$\rightarrow \mathrm{NH}(a\ ^1\Delta)+\mathrm{CO}(X\ ^1\Sigma^+). \quad (3)$$

In what follows, NH($X\ ^3\Sigma^-$) is denoted by ^{3}NH, and NH($a\ ^1\Delta$) by ^{1}NH. The origin of the optically bright state S_1 (at $< 35\,000\ cm^{-1}$) (Refs. 15–17) lies above the threshold to channel (1), but below that of channels (2) and (3).[10,13,14] At low excitation energies above the S_1 origin, intersystem crossing (ISC) to T_1 and internal conversion (IC) to S_0 are possible routes to channels (1) and (2). The energetically lowest channel (1) is spin-forbidden and has only recently been observed by direct detection of ^{3}NH in 260–217 nm photolysis.[15(b)] The competition between the spin-allowed channels (2) and (3) on S_0 and S_1, as well as the relative importance of the spin-forbidden pathway, are not yet fully elucidated. Channel (2) is known to dominate just above the opening of channel (3); however, the importance of the latter gradually increases and its quantum yield is largest at wavelengths around 200 nm, with channel (2) being the second major pathway.[1–4,8,10,12,18] The exact branching ratios and their wavelength dependencies are still not known with certainty. Above the barrier to dissociation on S_1, competition between decomposition on S_1 and predissociation following radiationless decay to lower states is expected; moreover, state specific effects following vibrationally mediated photodissociation have recently been observed at excitation energies where dissociation on S_1 plays a significant role.[10]

Several previous studies of HNCO photodissociation were carried out at photolysis energies relevant to this work.[1–11,13,18,19] In most studies 300 K samples were used, and some interpretations might have been affected by the use of bond energies which were later revised.[14] Chandler and co-workers determined the energy disposal in ^{1}NH and CO following photolysis of 300 K HNCO at several wavelengths between 230 and 193 nm.[1–3] They found cold ^{1}NH rotational distributions, while the corresponding CO distributions were hotter and typical of those commonly obtained by the rotational reflection principle. The proposed mechanism was direct dissociation on a repulsive S_1 surface. However, the CO signal was contaminated by a contribution from channel (1) whose existence was unknown at that time. Very recent experiments of jet-cooled photolysis at 217.6 nm gave a recoil

[a]Present address: Joint Institute for Laboratory Astrophysics, University of Colorado, Boulder, Colorado 80309.
[b]Author to whom correspondence should be addressed; e-mail: reisler@chem1.usc.edu

anisotropy parameter $\beta=-0.7\pm0.2$ and showed clearly an inverted CO($\nu=0$) rotational distribution, peaking at $J=22$ with FWHM $\Delta J\sim15$.[9] The ^{1}NH photofragment yield spectrum in jet-cooled samples is structured, but many features are broad, and an underlying continuum is evident.[13]

The H+NCO channel following 193 nm photolysis of jet-cooled HNCO was studied by Zhang *et al.* using the high-Rydberg time-of-flight (HRTOF) method.[7] The NCO fragment was produced with substantial bending excitation (although the largest fraction of the available energy was found in relative translation) and $\beta=-0.85$ was reported. The dynamics was characterized as direct dissociation on a repulsive surface. Crim and co-workers, using 300 K HNCO samples, looked at this channel near its threshold and deduced, based on the electronic absorption spectrum,[11] a predissociation mechanism with significant deviations from statistical behavior in the NCO vibrational distribution; note however that an incorrect D_0(H+NCO) value was used. Zyrianov *et al.* examined the dissociation of jet-cooled HNCO near the threshold to channel (2) at ~260 nm,[13] and found that NCO was rotationally cold indicating no exit channel barrier. They suggested that dissociation at this wavelength was slow, as two-photon absorption competed effectively with channel (2) decomposition. Both the absorption and the NCO photofragment yield spectra exhibited narrow spectral features with rotationally resolved bands persisting even above the threshold of channel (2), and the linewidths exhibited state-specific effects probably reflecting the radiationless decay step. They favored a mechanism involving IC followed by predissociation on S_0. In 248 nm photolysis studies of 300 K HNCO, the angular distribution was nearly isotropic,[8] also in accordance with a predissociation mechanism.

Thus, despite its small size, HNCO exhibits rich photochemistry involving several PES's and surface crossings.[12,20] Previous results indicate a transition at higher photolysis energies from a mechanism dominated by radiationless decay followed by decomposition on lower surfaces (i.e., T_1 and S_0) to a mechanism dominated more and more by dissociation on S_1. The transition region and the details of the competitive dynamics need to be better understood. Studying the dynamics over a broad range of photolysis energies also affords examples of vibrational predissociation on PES's with either shallow (S_1,T_1) or deep (S_0) wells. Evidently, unraveling the complex dynamics of HNCO requires close interplay between theory and experiment, with the latter providing high quality, state-specific data that can serve as benchmarks for comparisons with theory.

In this publication we present results obtained by photofragment ion imaging of H and CO from HNCO and D from DNCO, as well as by laser induced fluorescence (LIF) of ^{1}NH from HNCO. In particular, we discuss the photodissociation on HNCO via pathway (3) at two photolysis energies, 43 455 cm^{-1} (230.1 nm) and 45 960 cm^{-1} (217.6 nm) which lie 690 and 3195 cm^{-1}, respectively, above the channel (3) threshold, and compare the results to dissociation via channel (2) at 243.1 nm, where only channels (1) and (2) are open. The results demonstrate the power of the photofragment ion imaging technique pioneered by Chandler and Houston,[21] which is capable of providing rapidly and efficiently correlated product state distributions, as well as state specific angular distributions.

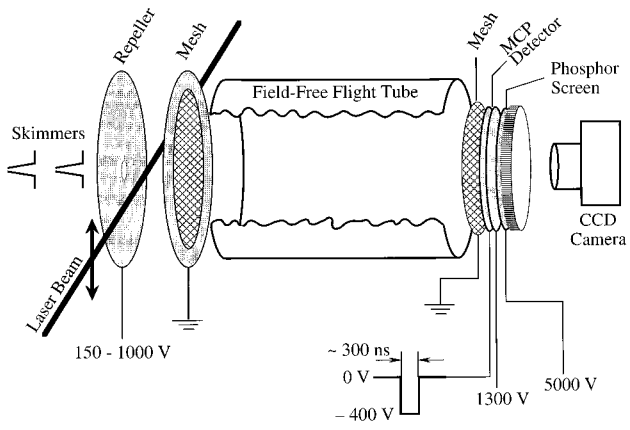

FIG. 1. Schematics of the photofragment ion imaging arrangement (not to scale).

II. EXPERIMENT

Our ion imaging arrangement, shown schematically in Fig. 1, is similar to that developed by Chandler and co-workers.[21] In brief, it consists of a single ion-acceleration stage, a field-free flight-tube and a position-sensitive detector. A doubly-skimmed (1.29 and 0.78 mm diam skimmers) pulsed molecular beam containing 2% H(D)NCO seeded in 1 atm of He enters the ion acceleration region through a 3 mm diam hole in the repeller plate. The rotational temperature in the skimmed beam was not determined directly, but based on the expansion conditions and previous results it is expected to be $\leqslant$5 K. The beam velocity vector is aligned along the ion flight-tube axis. H(D)NCO is photolysed with linearly polarized UV radiation ($\approx$0.3–2 mJ/pulse) generated by frequency-doubling the output of an excimer laser (Lambda Physik EMG 101 or 201) pumped dye laser (Lambda Physik LPD 3000 or FL 3002). The laser beam is focused with a 15 cm focal length lens and intersects the molecular beam at right angle, halfway between the repeller and extractor, the latter being a flat stretched piece of 333 lines per inch (lpi) Ni mesh mounted at the entrance of the flight-tube. The size of the overlap region of the laser and molecular beam is $\approx1.0\times0.2\times0.2$ mm^3. H(D) atoms from H(D)NCO photodissociation are detected by 2+1 resonance-enhanced multiphoton ionization (REMPI) via the $2\,^2S\leftarrow\leftarrow1\,^2S$ transition at 243.1 nm ($\leftarrow\leftarrow$ denotes a virtual two-photon transition), while CO fragments are interrogated by 2+1 REMPI via the Q-branches of the $B\,^1\Sigma^+\leftarrow\leftarrow X\,^1\Sigma^+$ or $C\,^1\Sigma^+\leftarrow\leftarrow X\,^1\Sigma^+$ transitions at 230.1 and 217.6 nm, respectively. In all cases the same laser pulse is used for H(D)NCO photolysis and H, D or CO REMPI detection. Ions are accelerated by the electric field into the 60 cm long flight-tube terminated by the 40 mm diam microchannel plate (MCP) detector (Galilleo, Inc.). Another 333 lpi Ni mesh shields the flight-tube from stray electric fields arising

from high voltages applied to the detector. The fine mesh in front of the detector does not result in imaging of the grid pattern, as 333 lpi translates into 524 lines of mesh per detector diameter, or >1 line per CCD camera pixel. The laser polarization vector is oriented parallel to the plane of the detector. The output of the MCP particle-multiplier is coupled to a phosphor screen, and the image generated by the ions impacting the detector is recorded with a thermoelectrically cooled CCD camera (Princeton Instruments, Inc.; back-illuminated 512×512 pixel array). Signal averaging is accomplished by accumulating images on the CCD array for $1–2\times10^4$ laser firings.

In order to discriminate against products from multiphoton dissociation in these one-laser experiments, the experimental conditions were set to discriminate against high-translational energy products. All the data were modeled successfully using the known energetics of HNCO decomposition, and no high velocity fragments were evident.

The global rotational distribution of ^{1}NH from HNCO photodissociation was measured in a separate apparatus[22] as described previously.[13] Jet-cooled HNCO was photolyzed at 217.6 nm and ^{1}NH products were probed by laser-induced fluorescence (LIF) under nonsaturated conditions via the $c\ ^1\Pi \leftarrow a\ ^1\Delta$ transition using a second laser. The observed spectral line intensities were normalized by the rotational line strength factors to yield J_{NH}-level populations.

The preparation of H(D)NCO followed the procedure of Ashby and Werner,[23] which involves the dropwise addition of a saturated aqueous (H_2O or D_2O) solution of potassium cyanate (KNCO) to concentrated phosphoric acid (85% H_3PO_4 in H_2O or D_3PO_4 in D_2O) under vacuum. The H(D)NCO vapor produced in this reaction was condensed in a liquid nitrogen trap and distilled twice between traps at -20 °C and -78 °C to remove mostly CO_2, NH_3, and H_2O impurities. DNCO experiments were blind to possible impurities of HNCO since the laser frequency was tuned to the D atom transition.

III. RESULTS AND ANALYSIS

Shown in Fig. 2(a) is an image obtained by monitoring the recoil of H atoms from HNCO photodissociation at 243.1 nm (41 141 cm^{-1}). The observed image is a 2D projection of the 3D photofragment recoil distribution. In this one-laser experiment, both HNCO dissociation and H atom detection were carried out at the same frequency. However, in order to cover the entire Doppler width of the recoiling H atoms the laser was scanned over a range of $\approx 3\ cm^{-1}$ while collecting the image.

Figure 2(b) displays an image obtained under similar conditions by monitoring D atoms from the photolysis of DNCO at approximately the same wavelength. As a result of the frequency shift between the H and D transitions, the difference in excitation energies of HNCO and DNCO in these one-laser experiments is $\approx 11\ cm^{-1}$. To cover the entire Doppler width of the D atoms, the laser was scanned over a range of $\approx 2\ cm^{-1}$.

The planes of the images in Figs. 2(a) and 2(b) include

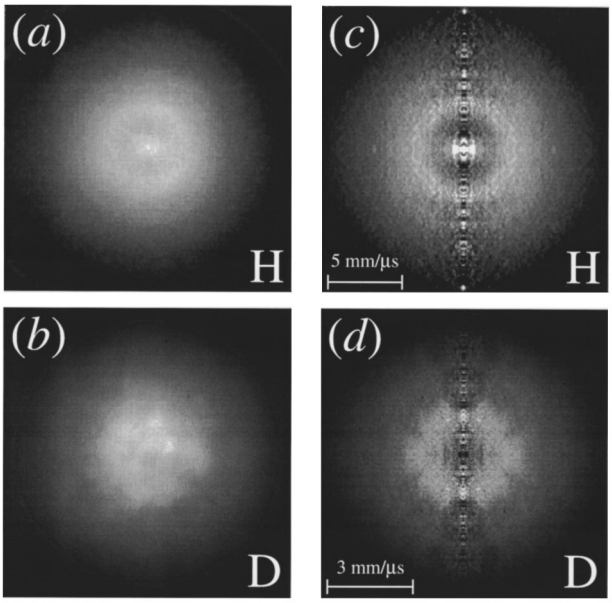

FIG. 2. (a) Experimental image of H atoms following 243.1 nm photolysis of HNCO. (b) Corresponding image of D atoms from DNCO. In both cases, the laser polarization is vertical in the figure plane. In (c) and (d) 2D cuts through 3D recoil distributions of H and D products, respectively, reconstructed by Abel inversion from images (a) and (b), respectively, are shown. Approximate center-of-mass velocity scales are indicated.

the cylindrical symmetry axes of the 3D ion clouds (vertical in the figures), as defined by the laser polarization. Clearly, the H and D atom recoil velocity distributions do not reveal significant deviations from spherical symmetry. The intensity distributions peak close to the respective image centers [i.e., at small H(D) atom velocities] indicating significant internal excitations of the NCO partner fragments. The experimental 2D projections were transformed into the 3D distributions by means of the Abel inversion as described elsewhere.[21,24] Because of the cylindrical symmetry inherent in the dissociation when the photolysis laser is linearly polarized, the reconstructed 3D distributions can be represented by 2D slices containing the symmetry axes, as shown in Figs. 2(c) and 2(d) for H and D, respectively. The complete 3D distributions can be obtained by rotating the cuts about their symmetry axes. The vertical lines (coinciding with the symmetry axes) visible in Figs. 2(c) and 2(d) are caused by noise accumulated in the process of the inverse Abel transformation.[21] Owing to the small spatial extent of the overlap between the molecular and laser beams, no deconvolution to account for the finite overlap volume (''deblurring'')[21(b)] was used. The 3D distributions of the H and D products were integrated to yield the angular distributions $P(\theta)$, plotted in Figs. 3(a) and 3(b), respectively, where θ is the angle between the recoil velocity and the laser polarization vector; also shown are fits by the standard recoil anisotropy function,[25]

$$P(\theta) \propto (2-\beta) + 3\beta \cos^2 \theta. \tag{4}$$

For H from HNCO, the best fit is obtained for a recoil anisotropy parameter $\beta = -0.13 \pm 0.05$. On the other hand, the

recoil distribution of D from DNCO is nearly spherically symmetric with only minor deviations near the cylindrical symmetry axis ($\theta \approx 0°$ and 180°). These deviations are artifacts resulting from the Abel inversion of the rather noisy image in Fig. 2(b) and are not significant. Fitting the data in the angular range θ=15°–165° gives $\beta=0.00\pm0.05$. For the perpendicular $A''\leftarrow A'$ transition,[16] negative values of β are expected if dissociation is fast on the time scale of parent rotation, with a limiting value $\beta=-1.0$.

At 230.1 nm (43 455 cm^{-1}), an image of CO produced via channel (3) was recorded by monitoring the Q-bandhead of the CO $B\ ^1\Sigma^+\leftarrow\leftarrow X\ ^1\Sigma^+$ transition, whose wavelength coincides with the photolysis wavelength. As individual CO rotational lines could not be resolved due to spectral congestion, a range of low J's ($J_{CO} \approx 0-4$) was probed at a fixed laser frequency. The experimental image shown in Fig. 4(a) was transformed into its 3D recoil distribution as described above, and a 2D cut through the reconstructed 3D distribution is displayed in Fig. 4(b). The angular distribution $P(\theta)$ and its fit are plotted in Fig. 5(a). The fit gives $\beta=-0.66\pm0.08$, and indicates a dissociation lifetime comparable to the time scale of parent rotation. As the Q-branch line strengths of the $^1\Sigma^+\leftarrow\leftarrow{}^1\Sigma^+$ transitions are independent of alignment factors,[26] the observed CO fragment angular distribution reflects only the effect of the $\boldsymbol{\mu}\bullet\mathbf{v}$ correlation, convoluted with parent lifetime.

Since at λ=230.1 nm the excitation energy is close to the opening of channel (3), the analysis of the product translational energy distribution $P(E)$ allows an accurate determination of $D_0(^1\mathrm{NH}+\mathrm{CO})$. The 3D distribution whose 2D cut is shown in Fig. 4(b) was integrated to obtain the radial distribution $P(r)$, where r is the distance from the HN–CO center of mass in 3D space. As the time allowed for recoil before product ions arrive at the detector (i.e., the ion flight-time) is measured experimentally, $P(r)$ is readily converted to the velocity distribution $P(v)$ and then to the ^{1}NH+CO translational energy distribution $P(E)$. Analysis of $P(E)$, following the procedure described below for the analysis of the 217.6 nm images, places $D_0(^1\mathrm{NH}+\mathrm{CO})$ at 42 765±25 cm^{-1}, as shown in Fig. 5(b). Although lower by 75 cm^{-1}, this value is within the error margin of our previous determination of $D_0(^1\mathrm{NH}+\mathrm{CO})$ based on LIF detection of ^{1}NH from jet-cooled HNCO, $42{,}840^{+10}_{-60}$,[13] and agrees very well with the 42 710±100 cm^{-1} value obtained by Brown *et al.* in double-resonance photolysis of 300 K samples.[10] This new value is used in all the data analyses reported in this work.

As seen even by visual inspection of Fig. 4 and confirmed by analysis of $P(E)$, CO (low-J's) is produced with relatively high average translational energy. Thus, ^{1}NH correlated with low J's of CO is rotationally cold, in agreement with the global ^{1}NH distributions obtained in HNCO photolysis in this energy range,[13,15(b)] Estimates show that the average ^{1}NH rotational energy $\langle E_{rot}(\mathrm{NH})\rangle$ correlated with CO($J \approx 0-4$) is only 60 cm^{-1}, or less than 10% of the total available energy.

Figures 6(a)–6(c) show representative examples of one-laser photofragment images obtained near 217.6 nm by monitoring the Q-branch of the CO $C\ ^1\Sigma^+\leftarrow\leftarrow X\ ^1\Sigma^+$ transition. The variation in the photolysis energy due to the spectroscopic selection of different CO levels (J=0–30) was <10 cm^{-1}. Figure 6(a) displays an image of CO($\nu=0$, J=0–4), obtained by monitoring the congested Q-bandhead. Since the vibrational frequencies of CO ($C\ ^1\Sigma^+$) and CO($X\ ^1\Sigma^+$) are very similar, the Q-bandheads of the (1-1) and (0-0) $C\ ^1\Sigma^+\leftarrow\leftarrow X\ ^1\Sigma^+$ tran-

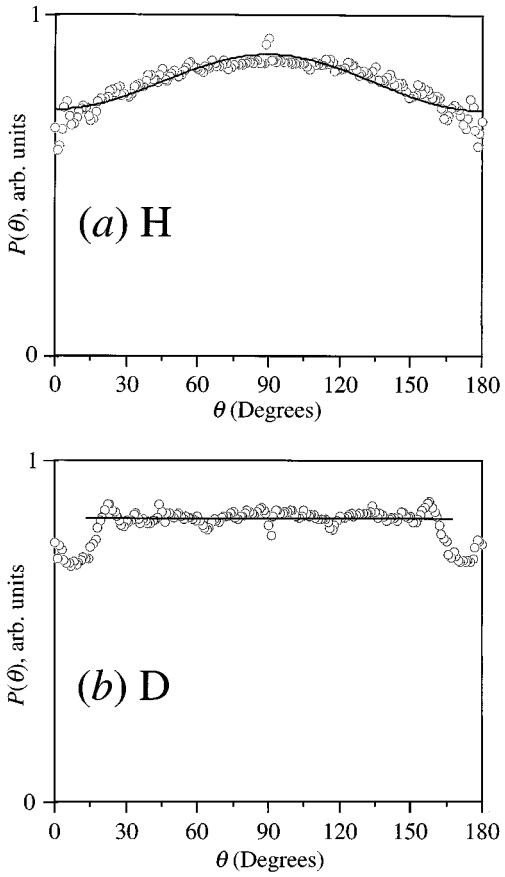

FIG. 3. Angular recoil distributions $P(\theta)$ (open circles) of H (a) and D (b) from photodissociation of H(D)NCO at 243.1 nm and their fits (solid lines) using the recoil anisotropy function [Eq. (1)], yielding $\beta=-0.13$ and 0.00 for H and D, respectively.

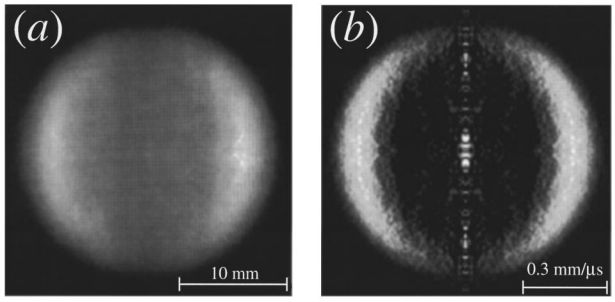

FIG. 4. (a) Experimental image of CO($\nu=0$, $J\approx0$–4) following 230.1 nm photolysis of HNCO. The actual scale of the image, recorded with a CO^+ flight-time of 25.7 μs, is indicated. The laser polarization is vertical in the figure plane. (b) 2D cut through the 3D recoil distribution reconstructed by Abel inversion from image (a). The center-of-mass velocity scale is indicated.

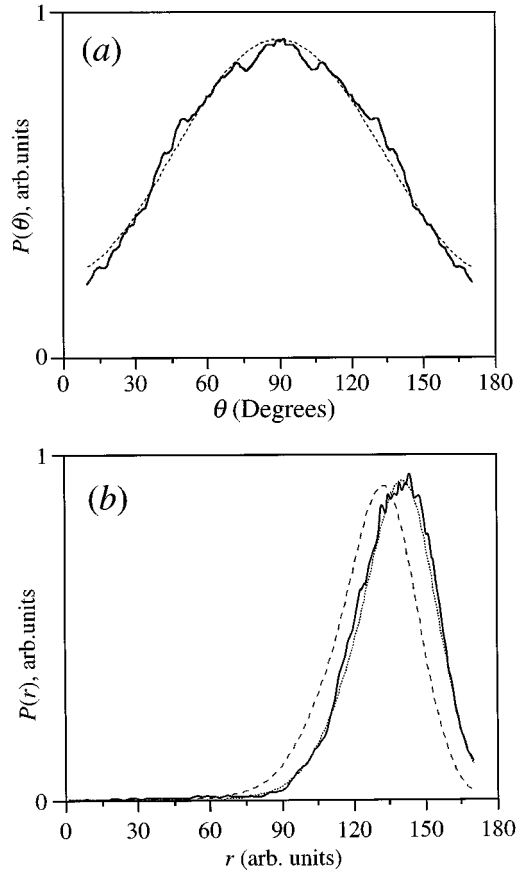

FIG. 5. (a) Angular recoil distribution $P(\theta)$ (solid line) of CO from the photodissociation of HNCO at 230.1 nm and its fit (dashed line) using the recoil anisotropy function [Eq. (1)] with $\beta=-0.66$. (b) Radial distribution $P(r)$ of CO from the photodissociation of HNCO at 230.1 nm and its fit (dotted line) assuming $D_0(^1\mathrm{NH+CO})=42\ 765\ \mathrm{cm}^{-1}$ (see text for details); the dashed line shows a fit with the same parameters but using $D_0(^1\mathrm{NH+CO})=42\ 840\ \mathrm{cm}^{-1}$ (Ref. 13).

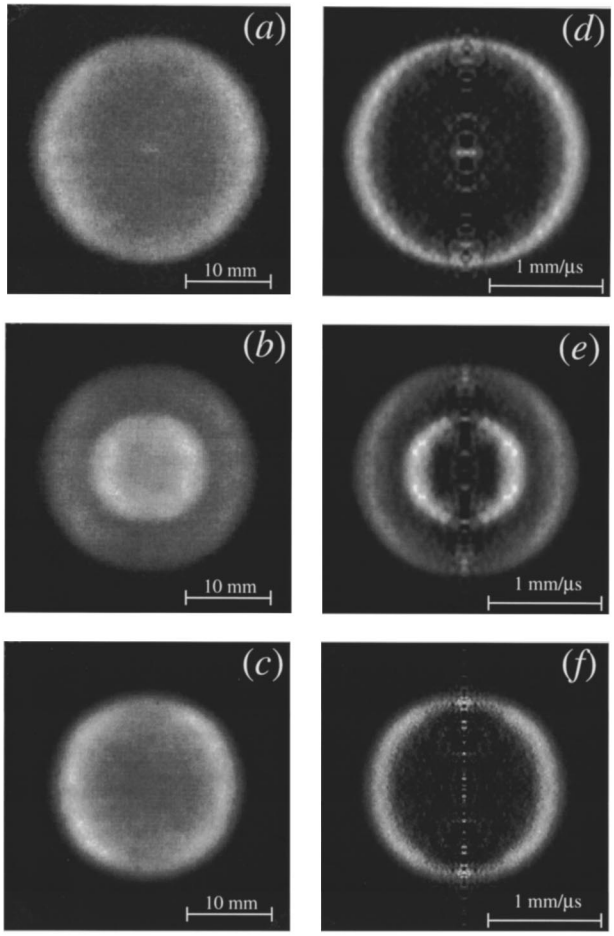

FIG. 6. (Left column) Representative experimental images of CO from HNCO photodissociation at 217.6 nm. (a) CO($\nu=0$, $J\leqslant 4$); (b) CO($\nu=0$, $J=15$) (outer ring) and CO($\nu=1$, $J=11$) (inner ring); (c) CO($\nu=0$, $J=22$). The actual scales of the images, recorded with a CO^+ flight-time of 13.2 μs, are indicated. In all cases, the laser polarization is vertical in the figure plane. (Right column) 2D cuts (d)–(f) through 3D recoil distributions reconstructed by Abel inversion from images (a)–(c), respectively. The center-of-mass velocity scales are indicated.

sitions are separated by only 1.2 cm^{-1}.[27] This proximity leads to spectral overlap in the 2+1 REMPI spectrum; i.e., CO($\nu=1$) is superimposed on CO($\nu=0$, $J\geqslant 10$). However the difference of $\approx 2100\ \mathrm{cm}^{-1}$ in the translational energies available to CO $\nu=0$ and 1 results in a clear spatial separation of their contributions in the images. Indeed, images recorded in the range of the spectral overlap exhibit a characteristic double-ring pattern as seen in Fig. 6(b) for CO($\nu=0$, $J=15$) (outer ring) superimposed on CO($\nu=1$, $J=11$) (inner ring). Figure 6(c), in turn, shows an image recorded for CO($\nu=0$, $J=22$), which overlaps the CO($\nu=1$, $J=19$) transition. This $\nu=1$ rovibrational level is apparently not populated in the photolysis, and the image exhibits a single ring pattern again. Note that $^1\mathrm{NH}(\nu=1)$ is not accessible at this photolysis energy.

The images recorded at 217.6 nm [Figs. 6(a)–6(c)] appear less anisotropic than those at 230.1 nm. This observation is confirmed by inspecting 2D cuts through the corresponding 3D distributions (reconstructed by Abel inversion) shown in the right column of Fig. 6 [panels (d)–(f)]. However, this is an artifact caused by incomplete integration over the full extent of the Doppler profile for each J_{CO}. Inspection of images obtained at slightly different wavelengths within the same J_{CO} indicates that the laser bandwidth is somewhat narrower than the full width of the CO product Doppler profiles. Due to the congested nature of the Q-branch of the CO $C\ ^1\Sigma^+ \leftarrow\leftarrow X\ ^1\Sigma^+$ transition, it is impossible to scan the laser fully across the Doppler profile of an individual rotational line without overlapping with neighboring lines. Since our goal was to obtain *correlated* rotational distributions, the probe laser wavelength was tuned only around the peak of each rotational transition, neglecting the wings, in order to minimize overlap. The smaller laser-exposure of the wings results in preferential detection of products recoiling at θ close to 0° and 180° and distorts the image anisotropy. We note, however, that the anisotropy in HNCO dissociation at 217.6 nm was recently measured by Kawasaki and co-workers who found $\beta=-0.7\pm0.2$.[9] This value is similar to that obtained by us at 230.1 nm, but one should exercise caution in comparing these two results as β is very sensitive to parent rotational temperature, which may

be somewhat different in the two experiments.

The left column of Fig. 7 [panels (a)–(c)] displays product translational energy distributions $P(E)$ obtained by transforming the radial distributions $P(r)$ associated with the 3D recoil distributions whose cuts are shown in Figs. 6(d)–6(f). Again, the distribution in Fig. 7(b) is clearly bimodal, apparently due to the fact that two rovibrational states of CO, i.e., CO(ν=0, J=15) and CO(ν=1, J=11), are probed simultaneously. Additional support for this interpretation [as opposed to interpreting the bimodal $P(E)$ as a consequence of a bimodal distribution of ^{1}NH correlated with a single CO level] is found in the observation that the two maxima in $P(E)$ are indeed separated by $\approx$2000 cm^{-1}, i.e., the vibrational energy spacing in CO($X\ ^1\Sigma^+$) (2143.2 cm^{-1}).[28]

It is important to realize that $P(E)$ obtained by the Jacobian transformation of $P(r)$ reflects the convolution of the product translational energy distribution with a spatial broadening function. Note, for example, that the $P(E)$ plots shown in Figs. 7(a)–7(c) extend beyond the maximum allowed by energy conservation. These high-energy tails are due entirely to the limited spatial (velocity) resolution. However, some trends regarding the correlated ^{1}NH distributions can be seen even by visual inspection of the $P(E)$ plots. For example, for J_{CO} = 22 [Fig. 7(c)], $P(E)$ peaks at an energy corresponding to higher J_{NH}, compared to $P(E)$ for $J_{CO} \leqslant 4$ [Fig. 7(a)], suggesting that ^{1}NH distributions correlated with higher J_{CO} tend to have *less* relative population in the lowest J_{NH} than those correlated with low J_{CO}.

This observation is confirmed by the correlated ^{1}NH distributions $P(J_{NH})$ displayed in Figs. 7(d)–7(f), which were obtained by fitting the state-selected CO radial distributions $P(r)$ [or, equivalently, the velocity distributions $P(v)$] by linear combinations of the spatially broadened J_{NH}-specific distributions $P_j(r)$,

$$P_{\mathrm{mod}}(r) = \sum_j a_j P_j(r),$$

where $j \equiv J_{NH}$, $P_{\mathrm{mod}}(r)$ is the resulting fitting function and the array $\{a_j\} = P(J_{NH})$ is the correlated ^{1}NH distribution. For a specific J_{CO}, the positions of the maxima of individual J_{NH}-specific distributions $P_j(r)$ are determined by energy conservation while their shape, resulting from the spatial broadening, is assumed Gaussian with a width adjusted to fit the ''fast'' slope in the experimental distribution $P(r)$.[29]

Although the extraction of the correlated J_{NH} distributions is not mathematically unique, sensitivity checks show that the procedure represents faithfully the general shapes of the distributions (see below). The ^{1}NH distributions correlated with low J's of CO(ν=0) have distinct maxima at the lowest J_{NH} [e.g., Figs. 7(d), 7(e)]. They also exhibit a second, less intense, feature at higher J_{NH} with a cutoff below the energetic limit [indicated by arrows in Figs. 7(d)–7(f)]. The ^{1}NH distributions correlated with higher J_{CO} become somewhat warmer with maxima shifted to J_{NH}=3, as illustrated in Fig. 7(f) for CO(ν=0, J=22), and J_{NH} populated almost up to the energetic limit. The correlated ^{1}NH distributions for CO(ν=1) are also cold, peaking at J_{NH} = 2, as shown in Fig. 7(e) for CO(ν=1, J=11). However, all distributions correlated with CO(ν=1) span almost the entire range of the energetically allowed J_{NH} (with a possible exception of the last allowed level).

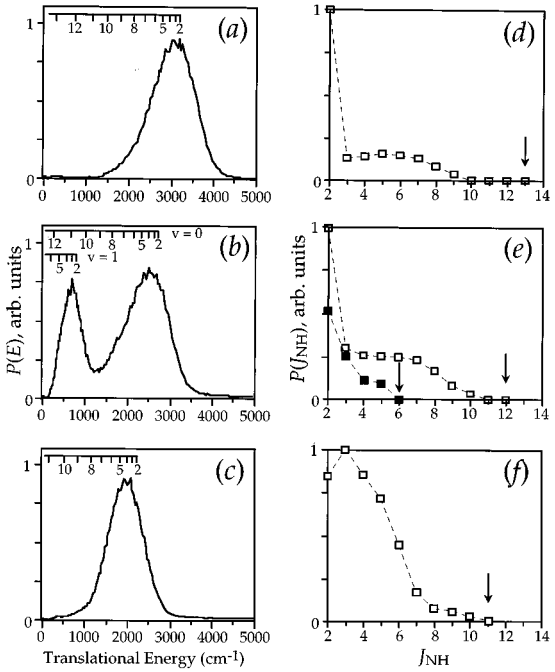

FIG. 7. (Left column) (a)–(c) Translational energy distributions $P(E)$ corresponding to the images in Figs. 6(a)–6(c), respectively, obtained in 217.6 nm photolysis of HNCO. Tic marks above the plots indicate the positions of correlated ^{1}NH rotational levels. In panel (b) the top comb relates to ^{1}NH correlated with CO(ν=0, J=15), while the lower comb is for ^{1}NH correlated with CO(ν=1, J=11). (Right column) Correlated ^{1}NH rotational distributions (d)–(f) extracted by fitting the state-selected CO radial distributions obtained from the images in Figs. 6(a)–6(c), respectively. Arrows mark the highest energetically allowed J_{NH}.

From the integrated images, we estimate that the CO ν=1/ν=0 branching ratio in HNCO photolysis at 217.6 nm is $\sim$0.1. Although CO(ν=1) in rotational levels up to J_{CO}=22 is accessible energetically, we do not observe significant populations for CO(ν=1, J>16).

CO photofragment images and correlated ^{1}NH rotational distributions such as those shown in Figs. 6 and 7(d)–7(f), respectively, were obtained for other CO rovibrational levels as well, encompassing the full range in which CO(ν=0, 1) populations were significant. CO in ν=0 was probed at 10 different J's ranging from 0 to 30 (J_{max}=40); for CO(ν=1) measurements were performed at 5 different J's ranging from 0 to 17 (J_{max}=22). Figure 8 shows a sum of the correlated ^{1}NH distributions (filled squares) weighted as per the global CO distribution obtained in 217.6 nm HNCO photolysis,[9] and compares it to the global ^{1}NH distribution (open circles) measured by LIF. Note the nearly quantitative agreement between the two distributions; both peak at J_{NH}=2, decrease rather monotonically with increasing J_{NH} and vanish for J_{NH}>10. The small discrepancy can be due to (i) incomplete selection of probed CO levels included in the weighted sum; (ii) a slightly higher detection sensitivity for

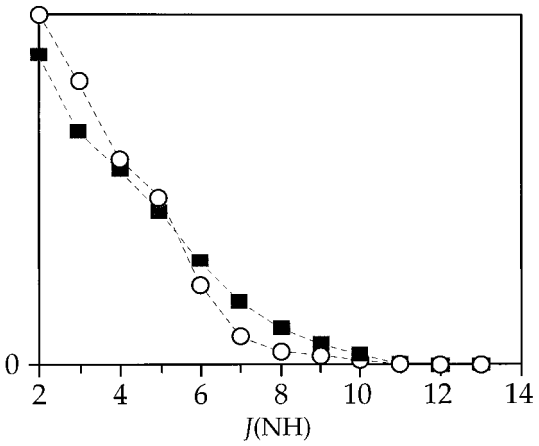

FIG. 8. (Filled squares) Sum of 15 correlated ^{1}NH rotational distributions extracted from 217.6 nm CO photofragment images and weighted as per the global CO distribution taken at the same wavelength (Ref. 9). (Open circles) The global rotational distribution of ^{1}NH in HNCO photodissociation at 217.6 nm measured by LIF.

slow CO in the imaging experiment as a consequence of incomplete integration over the Doppler profiles of CO transitions; and (iii) the nonunique nature of the J_{NH} fits. The good agreement with the global distribution confirms the validity of the fitting procedure used here to extract correlated ^{1}NH rotational distributions.

IV. DISCUSSION

A. H(D)+NCO at 243.1 nm

Understanding the mechanism of HNCO dissociation is closely interrelated with discerning the relative roles of S_0, S_1, and T_1. It appears that predissociation on S_0 is the dominant mechanism of decomposition via channel (2) from its threshold at 260.5 nm (38 370 cm^{-1}) up to at least 243 nm.[13] This conclusion is further supported by the lack of significant recoil anisotropy in the H+NCO channel at 248 nm (Ref. 8) and, as reported here, in the H(D)+NCO channel in dissociation of H(D)NCO at 243.1 nm.

The small values of the anisotropy parameter suggest lifetimes of many picoseconds, consistent with RRKM estimates for dissociation on S_0 via a reasonably tight TS.[30] We note that a similar trend in β parameters for HNCO and DNCO was recently observed with 300 K samples at 248 nm.[8] There are three potential sources that can contribute to the lower value of β for DNCO at 243.1 nm. First, although the photon energies in the two experiments are similar, the difference in HNCO and DNCO zero-point energies results in available energies of 2760 cm^{-1} and 2250 cm^{-1}, respectively, i.e., a difference of $\sim$500 cm^{-1}.[31] Second, the parent S_0 density of states in DNCO is higher than that in HNCO. Note that the TS frequencies in H–NCO and D–NCO are not very different, since it is the H(D)–N bond that is being broken. These two considerations result in $k_{HNCO}/k_{DNCO} \approx 2$, as estimated by RRKM calculations.[30] Third, the coupling matrix elements involved in the radiationless decay can differ substantially for HNCO and DNCO.[32]

The H atom image reveals some structure corresponding to vibrations of the NCO counter fragment, which is seen more clearly in the Abel-inverted image [Fig. 2(c)]. The central peak (which accounts for only a small fraction of the total yield) corresponds by energy conservation to the NCO (050) bending level, while the first ring surrounding it corresponds energetically to the (040), (120) or (011) levels. The results of Crim *et al.* suggest that NCO combination bands are weaker compared to bands of pure bending levels,[11] and thus the ring in the H atom image is more likely to result from the (040) level. Although vibrational assignments in NCO are complicated by the Renner–Teller interactions,[33,34] the mere fact that vibrations are partially resolved implies a modest rotational excitation of NCO. This observation agrees with previous results obtained in HNCO photolysis at other excitation energies,[7,11] and can be understood in part based on considerations of angular momentum conservation. Since in the jet-cooled HNCO rotational excitation is low, the rotational angular momentum of NCO must be matched by orbital angular momentum, which cannot be very large due to the small reduced mass of the H+NCO system.[7] Note that the structure in the D atom image [Figs. 2(b) and 2(d)] is less pronounced, possibly reflecting higher rotational excitation of NCO coming from DNCO (compared to that from HNCO), as is plausible considering the larger mass of D. Another possible source of the loss of resolution in the photolysis of DNCO is a more statistical population of the NCO vibrational levels.

B. ^{1}NH+CO at 230.1 nm

Less certain is the mechanism of HNCO decomposition near the threshold of channel (3). While H+NCO products can in principle be accessed on all three PES's (S_0, S_1, and T_1), ^{1}NH+CO can only be produced on S_0 and S_1. Since these surfaces have significant wells, indirect dissociation occurs in both cases. Thus, the differences in mechanisms are subtle, and the final outcome will depend on the rate of IC, the extent of intramolecular vibrational redistribution (IVR), different densities of states on S_0 and S_1 and possible potential barriers. It is expected that above the S_1 barrier, dissociation on this PES will progressively increase in importance, although dissociation on other surfaces will not be turned off immediately. Calculations performed in a 3D coordinate space indicate barriers on S_1 in both the H+NCO and ^{1}NH+CO channels, but their exact heights are still uncertain. The former barrier is estimated to be 6000–8000 cm^{-1}, while the latter is under 1000 cm^{-1}.[12,35]

The longest wavelength at which significant anisotropy in HNCO photodissociation has been observed so far is 230.1 nm [690 cm^{-1} above $D_0(^1\text{NH}+\text{CO})$], while 243.1 nm is the shortest wavelength where the angular distribution is still rather isotropic. Thus, the energy range between 243 and 230 nm promises to provide clues as to the relative roles of the different PES's. At present, it is not known if with 230.1 nm photolysis the S_1 barriers either to H+NCO or to ^{1}NH+CO are exceeded. The anisotropy parameter $\beta = -0.66 \pm 0.08$ measured at 230.1 nm corresponds, according to the

model of Jonah,[36,37] to $\tau_{dis}=1-2$ ps (for $T_{rot}=3-10$ K), if recoil is axial and deviations from the limiting value $\beta=-1$ are due solely to parent lifetime. Although quite fast on the time scale of parent rotation (and thus *consistent* with dissociation on S_1), this rate *does not preclude* predissociation on S_0. In fact, the observed anisotropy may reflect the cumulative decomposition rate on S_0 via *all* open channels.[38] At this energy, i.e., 5085 cm^{-1} above $D_0(H+NCO)$, decomposition via channel (2) is still the dominant channel,[10] and its rate on S_0 can be as fast as few picoseconds, depending on the geometry and location of the TS.[30] Thus, if the IC rate is faster than the unimolecular reaction rate, substantially negative values of β can be expected for predissociation on either S_0 or S_1. Note that the very slow increase in the ^{1}NH yield compared to the NCO yield near the threshold of channel (3) is also suggestive of competitive dissociation on the same PES.[13]

As with anisotropy, the interpretation of a rotationally cold ^{1}NH distribution at 230.1 nm is ambiguous. Recall that at its threshold, ^{1}NH is produced only in its lowest rotational level and no evidence of a barrier is seen.[13] The rotational distribution at 230.1 nm [$\langle E_{rot}\rangle \approx 60$ cm^{-1} for ^{1}NH correlated with CO($J \approx 0-4$), or $\langle E_{rot}\rangle \approx 30$ cm^{-1} for the global ^{1}NH distribution measured by LIF in this photolysis energy region][15(b)] is colder than predicted by phase space theory (PST).[39] This can reflect incomplete energy exchange between CO and NH rotations due to the large mismatch between the rotational constants ($B_{NH}=16.45$ cm^{-1}, $B_{CO}=1.93$ cm^{-1}). It may also reflect dynamical constraints on angular momentum or mapping of bending wave functions of a tight TS. At 690 cm^{-1} above $D_0(^1NH+CO)$, the TS of a barrierless reaction on S_0 may have already tightened considerably, giving rise to rotational distributions which deviate significantly from PST expectations. Measurement of the CO($X\ ^1\Sigma^+$) rotational distribution from channel (3) is complicated, since at 230.1 nm its yield from channel (1) is significantly larger;[15(b)] however, experiments that discriminate between fast and slow CO may enable the distinction between the contributions of these two channels.

C. ^{1}NH+CO at 217.6 nm

At higher energies, the ^{1}NH+CO barrier on S_1 is eventually exceeded and the excess energy at 217.6 nm (3.195 cm^{-1}) is above all current estimates of the height of this barrier.[20,35] Thus, decomposition on S_1 is expected to compete effectively with IC and ISC. However, the other surfaces (S_0, T_1) continue to participate, giving rise to a complex interplay between different PES's; for example, a small LIF signal from ^{3}NH (accessible only via ISC to T_1) is still observed.[15(b)]

The product state distributions at 217.6 nm exhibit clear dynamical biases. The correlated and global ^{1}NH distributions are cold, peaking at the lowest J_{NH}. The average rotational energy in ^{1}NH is $\langle E_{rot}(^1NH)\rangle \approx 215$ cm^{-1}, or about 0.07 of the available energy, as calculated from the global distribution. We note that cold ^{1}NH distributions have also been determined in the works of Chandler and co-workers following 300 K photolysis at 643, 3035, 5415, and 9529 cm^{-1} above $D_0(^1NH+CO)$.[2] In contrast, the CO($X\ ^1\Sigma^+$) rotational distribution measured by Kawasaki and coworkers is hot and bell-shaped with the maximum at $J_{CO}\approx 22$, and $\langle E_{rot}(CO)\rangle \approx 840$ cm^{-1}.[9] Although this estimate does not take into account the contribution of CO($\nu=1$) to the REMPI spectrum, we estimate that the correction due to the ~10% yield of CO($\nu=1$) does not exceed ~0.05 of $\langle E_{rot}(CO)\rangle$. Thus, about 0.26 of the total available energy is partitioned into CO rotation, while the average vibrational energy, $\langle E_{vib}(CO)\rangle \sim 200$ cm^{-1}, accounts for ~0.06 of the total. CO is more internally excited than ^{1}NH, while excitation of all product internal degrees of freedom accounts for ~0.4 of the total available energy with the rest going into translation. We note that because of the large mismatch in NH and CO rotational constants, the angular momentum of CO in high rotational levels cannot be compensated by NH rotation to satisfy angular momentum conservation, since the available energy allows a maximum of $J_{NH}=13$, while the maximum J_{CO} is 40. Therefore, significant values of L, the orbital angular momentum, are required to balance the product rotations, implying a substantial translational energy release.

Although the predominant decomposition mechanism at 217.6 nm is most likely vibrational predissociation on S_1, the energy partitioning deviates substantially from PST predictions, and is dominated by dynamics. This is expected, since S_1 dissociation involves a barrier and a tight TS, and energy exchange in the exit channel may be incomplete. Supporting this point, the calculations of Fang *et al.* show that the TS on S_1 leading to ^{1}NH+CO is located at 1.952 Å along the C–N bond coordinate.[20] Franck–Condon considerations indicate that the repulsive slope along the N–C coordinate is accessed in the photoexcitation encouraging dominance of dynamics over statistics. In the absence of calculations on a realistic PES, we can only compare our results to relevant limiting models. Since the excess energy above $D_0(^1NH+CO)$ is only ~3200 cm^{-1} (and the energy available above the barrier may be even smaller), comparisons to the Franck–Condon (FC) model of mapping of TS wave functions, and to the rotational reflection principle are appropriate.[40–42]

The shapes of the correlated ^{1}NH distributions are consistent with mapping of the lowest H–N–C bending levels of the TS. Note that the shape of the wave function at the TS can be very different from that in the FC region.[42] In other words, even when the wave function in the FC region has a nodal structure, some or all of the nodes may vanish as it passes through a narrow bottleneck near the TS. For ^{1}NH correlated with CO in the lowest rotational levels, we can consider CO as an atom with no angular momentum, and carry out FC mapping calculations as for a triatomic molecule treating the H–N–C bend as a harmonic oscillator and assuming that the parent angular momentum is zero.[43] Although a gross oversimplication, this model is capable of reproducing the general shapes of the correlated ^{1}NH distributions when assuming no exit-channel torque and a ~300 cm^{-1} bending frequency at the TS (about half of the corre-

sponding ground state value). Such ''softening'' of the H–N–C bend is expected from purely geometrical considerations, i.e., the nearly 60% elongation of the C–N bond at the TS compared to the FC region.[20]

The situation is more complicated when ^{1}NH is correlated with high J_{CO}; to the best of our knowledge, the effect of counter fragment rotation has not yet been treated within the FC mapping model. If, however, we view the rotational angular momentum of CO as the counterpart of parent rotation in triatomic dissociation, some insight can be gained from FC-model calculations carried out for triatomic molecules at high parent J states within the framework of an infinite order sudden approximation.[44] These calculations show that parent rotation is partitioned unequally between product rotation and orbital angular momentum, and results in a broader range of fragment rotational excitation than in the case of low parent J.[44] Such broadening has also been observed experimentally in photodissociation of triatomic molecules which are well described by the FC model when comparing 300 K to jet-cooled samples.[41] By analogy, we can speculate that counter fragment CO rotation will result in broader correlated ^{1}NH distributions than that correlated with CO($J = 0$). This is indeed what is observed in our experiments [e.g., compare Figs. 7(d)–7(f)]. Additional support for the interpretation that the shapes of ^{1}NH distributions reflect mapping of H–N–C bending wave functions at the TS is found in the similarity between the ^{1}NH distributions correlated with CO(ν=0) and CO(ν=1). Note that for CO(ν=1), ^{1}NH distributions span almost the entire range of the energetically allowed J's, while most of those correlated with CO(ν=0) cut off below the energetic limit. Thus, the rotational excitation of ^{1}NH appears to be constrained by dynamics rather than energetics. The shapes of the H–N–C bending wave functions at the TS are likely to depend only weakly on CO vibrational excitation; the latter determines mostly how many levels can be populated at the TS, i.e., for ^{1}NH correlated with CO(ν=1) the rotational distribution will reflect mapping only of the lowest level of the TS, while for ^{1}NH correlated with CO(ν=0) some contribution from higher TS bending levels is also possible.[45]

Considering interactions beyond the TS, the momentum of any force exerted on NH during the C–N bond breaking will be small, since the NH fragment's center of mass lies very close to the N atom, almost on the line of force acting along the C–N bond. Thus, impulsive release will contribute little to ^{1}NH fragment rotational excitation beyond the extent of mapping of the H–N–C bending vibration in the TS region. The small magnitude of the impulsive torque, combined with little anisotropy on S_1 in the H–N–C bending coordinate, can explain why the NH populations peak at low J's. A more significant torque in the exit channel is expected to be exerted by the same force (directed along the C–N bond) on CO. This torque will be further modulated by the anisotropy in the N–C–O bending potential, and this can be modeled by the rotational reflection principle.[41] Such model reproduced well the CO rotational distributions obtained in 300 K photolysis of HNCO at 193 nm.[3(a)] As was pointed out before,[3,11] significant torque in the exit channel is more likely to arise in dissociation on S_1 than on S_0, because the TS in S_1 is bent (N–C–O angle 120.3°),[20] while on S_0 the NCO moiety is almost linear.

V. CONCLUSIONS

(1) The decomposition of H(D)NCO from the opening of the H(D)+NCO channel at 260 nm up to at least 243 nm proceeds via vibrational predissociation on S_0. This is supported by the near isotropy of the H and D angular distributions at 243 nm. At shorter wavelengths, a switch to a complex interplay between S_0 and S_1 dissociation pathways occurs.

(2) Substantial anisotropy is observed in the ^{1}NH+CO channel of HNCO at 230.1 nm. The corresponding increase in dissociation rate is consistent with the increase in rate of a unimolecular reaction on S_0, but direct dissociation on S_1 cannot be excluded. Therefore, the increase in anisotropy cannot be unambiguously attributed to a change in dissociation mechanism.

(3) At 217.6 nm, energy disposal in ^{1}NH+CO indicates that the dissociation is dominated by decomposition on S_1 (with some contribution from S_0). The available evidence is mostly circumstantial and more experimental and theoretical work is needed to clarify the details of the dynamics in this region. Product state distributions exhibit clear dynamical signatures; rotationally hot CO is produced in both energetically accessible vibrational levels (ν=0 and 1), while ^{1}NH correlated with specific rovibrational states of CO is always cold. Both the correlated and the global ^{1}NH distributions can be rationalized in terms of mappings of TS H–N–C bending wave functions with only modest torque in the exit channel. The differences between ^{1}NH and CO product distributions can be understood in terms of post-TS dynamics.

Finally, unraveling the relative roles of S_0, T_1, and S_1 in HNCO dissociation and the dynamics on each surface will evidently require close cooperation between theory and experiment. The results reported in this publication provide benchmarks for comparisons with theory, and also point towards ranges of photolysis energies where changes in mechanisms are likely to occur.

ACKNOWLEDGMENTS

We wish to thank David Chandler, Albert Heck, David Neyer, and Arthur Suits for helpful advice in setting up our imaging apparatus, and Aaron Katzenstein, a summer participant in USC's NSF-REU program, for his help in carrying out these experiments. We are also grateful to David Chandler for sharing with us the data analysis software, including the program used for Abel inversion of images. We thank R. Schinke, K. Morokuma, F. F. Crim, and H.-R. Volpp for sending us preliminary results and preprints. We benefited greatly from discussions with F. F. Crim, R. Schinke, S. Brown, J. Zhang, and C. Wittig. Support by the U.S. Army Research Office and the National Science Foundation is

gratefully acknowledged. Partial funds for the construction of the imaging setup were obtained from the Department of Energy.

[1] T. A. Spiglanin, R. A. Perry, and D. W. Chandler, J. Phys. Chem. **90**, 6184 (1986).
[2] T. A. Spiglanin and D. W. Chandler, J. Chem. Phys. **87**, 1577 (1987).
[3] (a) T. A. Spiglanin, R. A. Perry, and D. W. Chandler, J. Chem. Phys. **87**, 1568 (1987); (b) T. A. Spiglanin and D. W. Chandler, Chem. Phys. Lett. **141**, 428 (1987).
[4] W. K. Yi and R. Bersohn, Chem. Phys. Lett. **206**, 365 (1993).
[5] B. Bohn and F. Stuhl, J. Phys. Chem. **97**, 4891 (1993).
[6] B. Ruscic and J. Berkowitz, J. Chem. Phys. **100**, 4498 (1994).
[7] J. Zhang, M. Dulligan, and C. Wittig, J. Phys. Chem. **99**, 7446 (1995).
[8] (a) R. A. Brownsword, T. Laurent, R. K. Vatsa, H.-R. Volpp, and J. Wolfrum, Chem. Phys. Lett. **249**, 162 (1996); (b) **258**, 164 (1996).
[9] M. Kawasaki, Y. Sato, K. Suto, Y. Matsumi, and S. H. S. Wilson, Chem. Phys. Lett. **251**, 67 (1996).
[10] S. S. Brown, H. L. Berghout, and F. F. Crim, J. Chem. Phys. **105**, 8103 (1996).
[11] (a) S. S. Brown, H. L. Berghout, and F. F. Crim, J. Chem. Phys. **102**, 8440 (1995); (b) S. S. Brown, R. B. Metz, H. L. Berghout, and F. F. Crim, J. Phys. Chem. **100**, 7948 (1996); (c) J. Chem. Phys. **105**, 6293 (1996); (d) S. S. Brown, C. M. Cheatum, D. A. Fitzwater, and F. F. Crim, *ibid.* **105**, 10911 1996); (e) S. S. Brown, H. L. Berghout, and F. F. Crim, *ibid.* (in press).
[12] A. M. Mebel, A. Luna, M. C. Lin, and K. Morokuma, J. Chem. Phys. **105**, 6439 (1996).
[13] (a) M. Zyrianov, A. Sanov, T. Droz-Georget, and H. Reisler, R. Soc. Chem. Faraday Discuss. **102**, 263 (1995); (b) M. Zyrianov, T. Droz-Georget, A. Sanov, and H. Reisler, J. Chem. Phys. **105**, 8111 (1996).
[14] From Ref. 13(b), $D_0(^3\mathrm{NH}+\mathrm{CO}) = 30\,150 \pm 60\ \mathrm{cm}^{-1}$; $D_0(\mathrm{H}+\mathrm{NCO}) = 38\,370 \pm 30\ \mathrm{cm}^{-1}$; $D_0(^1\mathrm{NH}+\mathrm{CO}) = 42\,840^{+10}_{-60}\ \mathrm{cm}^{-1}$. From Ref. 10, $D_0(\mathrm{H}+\mathrm{NCO}) \leqslant 38\,320 \pm 140\ \mathrm{cm}^{-1}$; $D_0(^1\mathrm{NH}+\mathrm{CO}) = 42\,710 \pm 100\ \mathrm{cm}^{-1}$. We recommend the following bond enthalpies: $D_0(^3\mathrm{NH}+\mathrm{CO}) = 30\,150 \pm 60\ \mathrm{cm}^{-1}$ [Ref. 13(b)]; $D_0(\mathrm{H}+\mathrm{NCO}) = 38\,370 \pm 30\ \mathrm{cm}^{-1}$ [Ref. 13(b)]; $D_0(^1\mathrm{NH}+\mathrm{CO}) = 42\,765 \pm 25\ \mathrm{cm}^{-1}$ (this work).
[15] (a) M. Zyrianov, A. Sazonov, R. A. Beaudet, and H. Reisler (to be published); (b) Th. Droz-Georget, M. Zyrianov, A. Sanov, and H. Reisler, Ber. Bunsenges. Phys. Chem. (in press).
[16] R. N. Dixon and G. H. Kirby, Trans. Faraday Soc. **64**, 2002 (1968).
[17] H. Okabe, J. Chem. Phys. **53**, 3507 (1970); in *Photochemistry of Small Molecules* (Wiley–Interscience, New York, 1978).
[18] A. Tezaki, S. Okada, and H. Matsui, J. Chem. Phys. **98**, 3876 (1993).
[19] (a) W. S. Drozdoski, A. P. Baronavski, and J. R. McDonald, Chem. Phys. Lett. **64**, 421 (1979); (b) G. T. Fujimoto, M. E. Umstead, and M. C. Lin, Chem. Phys. **65**, 197 (1982).
[20] W.-H. Fang, X.-Z. You, and Z. Yin, Chem. Phys. Lett. **238**, 236 (1995).
[21] (a) D. W. Chandler and P. L. Houston, J. Chem. Phys. **87**, 1445 (1987); (b) A. J. R. Heck and D. W. Chandler, Annu. Rev. Phys. Chem. **46**, 335 (1995).
[22] A. Ogai, C. X. W. Qian, and H. Reisler, J. Chem. Phys. **93**, 1107 (1990).
[23] R. A. Ashby and R. L. Werner, J. Mol. Spectrosc. **18**, 184 (1986).
[24] R. N. Bracewell, in *The Fourier Transform and its Applications* (McGraw–Hill, New York, 1986).
[25] (a) R. N. Zare and D. R. Herschbach, Proc. IEEE **51**, 173 (1963); (b) R. N. Zare, Mol. Photochem. **4**, 1 (1972).
[26] R. G. Bray and R. M. Hochstrasser, Mol. Phys. **31**, 1199 (1976).
[27] S. M. Koeckhoven, W. J. Buma, and C. A. de Lange, J. Chem. Phys. **99**, 5061 (1993).
[28] K. P. Huber and G. Herzberg, in *Molecular Spectra and Molecular Structure* (Van Nostrand, Princeton, 1979), Vol. 4.
[29] The rationale behind performing fits in r-space, as opposed to E-space, is that the major source of experimental broadening is the finite size of the dissociation/ionization volume. Its size, defined by the intersection of laser and molecular beams, corresponds to the width of the broadening function, which is independent of J_{NH} and J_{CO} in r-space.
[30] In these estimates, the H–NCO TS frequencies were assumed to include those of free NCO, i.e., 1290, 2338, and $\approx 500\ \mathrm{cm}^{-1}$ (C–N and C–O stretches and NCO bend, respectively), and $\approx 100\ \mathrm{cm}^{-1}$ for both the in-plane and out-of-plane H(D)–N–C bending vibrations. The parent density of states was estimated by direct harmonic count. The difference between HNCO and DNCO was accounted for by replacing the frequency of the N–H stretch ($3538\ \mathrm{cm}^{-1}$) by that of N–D ($2637\ \mathrm{cm}^{-1}$), while leaving other frequencies unchanged, as the corresponding frequencies of the TS are expected to change accordingly, canceling out the isotope effect of all but the N–H(D) stretching vibrations in the RRKM equation.
[31] A. L. L. East, C. S. Johnson, and W. D. Allen, J. Chem. Phys. **98**, 1299 (1993).
[32] E. S. Medvedev and V. I. Osherov, in *Radiationless Transitions in Polyatomic Molecules* (Springer, Berlin, 1995), Vol. 4.
[33] J. T. Hougen, J. Chem. Phys. **36**, 519 (1961).
[34] D. Patel-Mistra, D. G. Sauder, and P. J. Dagdigian, J. Chem. Phys. **93**, 5448 (1990).
[35] R. Schinke, J. Klossika, H. Floethmann, and K. Yamashita (to be published).
[36] C. Jonah, J. Chem. Phys. **55**, 1915 (1971).
[37] S. Yang and R. Bersohn, J. Chem. Phys. **61**, 4400 (1974).
[38] If deviations from the limiting value of $\beta = -1$ are due solely to parent lifetime, then these deviations are a measure of the monitored product appearance time. Therefore, if decomposition via channels (2) and (3) occurs on S_0 and IC is much faster than the subsequent unimolecular reaction, then β measured in the CO channel reflects the cumulative rate of these two channels, $k_2 + k_3$. The same is true if both channels evolve mainly on S_1. On the other hand, if the IC rate (k_{IC}) is smaller than $k_2 + k_3$ *and barriers on* S_1 *are not exceeded*, then β of CO is essentially a measure of k_{IC}. Only if channels (2) and (3) evolve on different PES's will β of CO reflect the rate of channel (3) alone; in this case the IC step would effectively uncouple the two rates from each other since the probability of recrossing from S_0 back to S_1 is small based on relative densities of states considerations.
[39] (a) P. Pechukas, J. C. Light, and C. Rankin, J. Chem. Phys. **44**, 794 (1966); (b) P. Pechukas and J. C. Light, *ibid.* **42**, 3281 (1965); (c) J. C. Light, Discuss. Faraday Soc. **44**, 14 (1967).
[40] C. X. W. Qian, A. Ogai, J. Brandon, Y. Y. Bai, and H. Reisler, J. Phys. Chem. **95**, 6763 (1991).
[41] R. Schinke, in *Photodissociation Dynamics* (Cambridge University Press, Cambridge, 1993).
[42] H. Reisler, H.-M. Keller, and R. Schinke, Comments At. Mol. Phys. **30**, 191 (1994).
[43] The simulations were carried out following the FC mapping formalism described in Ref. 40, which is based on J. A. Beswick and W. M. Gelbart, J. Phys. Chem. **84**, 3148 (1980).
[44] H. Grinberg, C. J. Williams, and K. F. Freed, J. Chem. Phys. **100**, 9215 (1994).
[45] A. Sanov, Ph.D. thesis, University of Southern California, 1996.